JOURNAL OF THERMOPHYSICS AND HEAT TRANSFER
Vol. 15, No. 3, July–September 2001

Heat Transfer to the Inclined Trailing Wall of an Open Cavity

Orval A. Powell*
Air Force Research Laboratory, Wright–Patterson Air Force Base, Ohio 45433-7251
and
Jeffrey P. Bons†
Air Force Institute of Technology, Wright–Patterson Air Force Base, Ohio 45433-7765

An experimental and computational investigation of a cavity geometrically similar to one currently being considered for use in a supersonic combustion ramjet engine was performed in a cold flow environment without fuel addition. The axial variation of heat transfer was determined in the form of Stanton number using temperature data recorded along the floor and inclined trailing wall of an open cavity exposed to a Mach 2.9 airflow. These results were compared to Stanton number calculations from recorded temperature data along a flat plate at two axial locations. Along the inclined trailing wall, the Stanton number increased both above and below the inclined trailing wall from the shear layer reattachment point. The experimental data suggest that the Stanton number increases were due to the conversion of energy from flow turning and flow recirculation, respectively. A schlieren flow visualization was performed that showed coalescing Mach waves forming an oblique shock above the trailing wall. For comparison, a two-dimensional Navier–Stokes computational evaluation was performed using a Reynolds' stress model for turbulence closure. These computational results displayed a similar trend in Stanton number within the cavity.

Nomenclature

A = temperature amplitude
c_f = skin-friction coefficient
c_p = specific heat
h = heat transfer coefficient
k = thermal conductivity
M = Mach number
p = pressure
Re = Reynolds number, $\rho V x/\mu$
St = Stanton number, $h/\rho_{\text{ref}} V_\infty c_{p,\text{ref}}$
T = temperature
t = time
V = velocity
x = axial direction
y = vertical direction
y^+ = wall coordinate
α = thermal diffusivity, $k/\rho c_p$
γ = ratio of specific heats
δ_t = turbulent boundary-layer thickness
μ = dynamic viscosity
ρ = density
ϕ = phase shift
ω = angular frequency, rad/s

Subscripts

acr = acrylic
aw = adiabatic wall
corr = corrected
i = initial
ref = reference
w = wall
x = based on axial direction
0 = stagnation
∞ = freestream

Presented as Paper 99-4889 at the AIAA 9th International Space Planes and Hypersonic Systems and Technology Conference, Norfolk, VA, 1–5 November 1999; received 28 March 2000; revision received 18 December 2000; accepted for publication 20 December 2000.

*High-Speed Systems Development Engineer, Propulsion Directorate; 1950 Fifth Street. Member AIAA.
†Assistant Professor, Department of Aeronautics and Astronautics, 2950 P Street. Member AIAA.

Introduction

RECENT programs, such as the National Aerospace Plane, NASA's Hyper-X, and the U.S. Air Force Hypersonic Technology Program (HyTech), have brought about a resurgence of interest in hypersonic technology. With this resurgence, there has been a great deal of research in all areas associated with hypersonic flight, from material design to thermal management to propulsion. Though all of these areas have seen considerable research activity, the propulsion system has been a focal point of a great deal of research. This concentration is due in part to the results of past work, such as the X-15 project, which achieved sustained flight at Mach 6.7 using a rocket propulsion system.[1] Current research programs, such as Hyper-X and HyTech, are striving for comparable flight Mach numbers (in excess of Mach 6) from an airbreathing (scramjet) propulsion system. The use of air is important because the oxidizer need not be carried onboard as in a rocket propulsion system, thereby lowering the required weight of the vehicle. However, at this flight speed, engine combustion would occur in a supersonic flow with residence times on the order of a millisecond or less. These short residence times can hinder or prevent complete mixing and combustion. In spite of these short residence times, the successful design of a scramjet propulsion system is key to achieving sustained hypersonic flight.[1]

Several researchers have evaluated the use of a recessed flame holder (cavity) to increase fuel–air mixing and residence times in a supersonic combustion chamber.[2–4] Although the use of a cavity affords low total pressure losses, there are high heat loads present in the cavity. The trailing wall of the cavity results in a stagnation region for the freestream flow, causing the flow to recirculate within the cavity. This recirculation causes the cavity to act as a flameholder. Fuel can mix with entrapped air in the cavity before being expelled into the main flow for the remaining submillisecond residence time. This premixing effectively increases the fuel residence time as it reacts with the small portion of entrapped air. However, the stagnation region caused by the trailing wall is a significant drawback of this design due to substantial conversion of kinetic energy to thermal energy. Current research has advanced active cooling technology (such as the use of endothermic fuels) to a level that should

be able to endure the high heat loads that will be present in a scramjet engine.[2] However, the amount of experimental data pertaining to heat loading in a cavity flow is limited. Therefore, the aim of the present research was to extend the cavity flow heat flux database and to increase the physical understanding of this complex flowfield. In addition, it was hoped that these data could also be used for validation of computational flow models applied to the supersonic cavity flowfield.

Experimental Setup

The present work used an inclined (20 deg to the horizontal) trailing wall in a cavity similar to that found in the literature[2,5,6] (Fig. 1). The wall downstream of the cavity was at the same height as the wall upstream of the cavity. The airflow separates over the cavity leading edge (LE) forming a free shear layer above the cavity before reattachment on the inclined trailing wall. The cavity cold flow tests were performed in the Air Force Institute of Technology's Mach 2.9 wind tunnel. The short duration test facility had a run time of approximately 25 s. The wind tunnel consisted of a plenum chamber, converging–diverging half nozzle, test section, diffuser, and evacuated chamber (Fig. 2). The sidewalls of the test section were constructed of acrylic plastic sheet for optical accessibility and to ensure thermal isolation from the aluminum test section floor and ceiling. Circular optical glass inserts were placed in each sidewall such that the cavity flowfield would be captured by the schlieren flow visualization technique.

The flow total (stagnation) properties, $T_0 = 295$ K and $p_0 = 0.287$ MPa, were measured downstream of a flow straightener and upstream of the nozzle throat (Fig. 2). The test section had a 6.35-cm-square cross section, a freestream Mach number of 2.85 ± 0.18, and a freestream turbulence level of 0.8% (Ref. 7). The relative effects of forced and free convection were assessed, and free convection effects were found to be negligible. A radiation analysis was also performed,[8] which showed that radiation heat transfer was $<1\%$ of the convective heat transfer. Hence, radiation effects were also neglected.

The data acquisition system consisted of a personal computer with an A/D system and 13 thermocouples. The sampling rate was 7.8 Hz, with approximately 200 points recorded during the 25-s tunnel operation. The accuracy of the A/D system and thermocouple arrangement was ± 1.3°C. (Refs. 9 and 10).

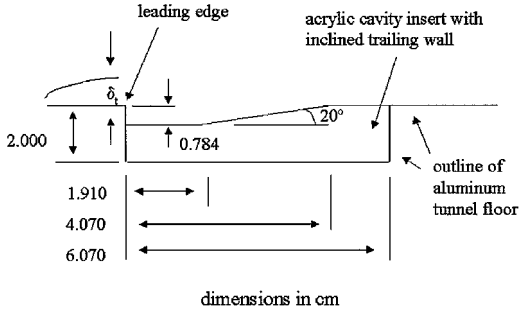

Fig. 1 Schematic of cavity and inclined trailing wall insert.

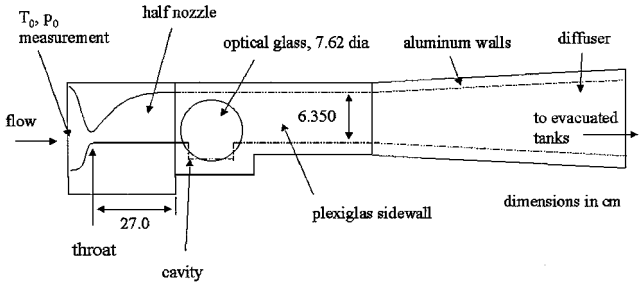

Fig. 2 Schematic of half nozzle and test section.

To simulate scramjet conditions faithfully, both the Reynolds and Mach numbers had to be matched to values tested by others in the open literature. The tunnel's design freestream Mach number of 2.9 is in the range of those projected for supersonic combustion chambers.[2–4] The freestream Reynolds number was measured by Latin[11] to be $Re_\infty = 1.9 \times 10^7$ m^{-1} for $T_0 = 293$ K and $T_{aw} = 275$ K at the design Mach number. This Reynolds number measurement was used to determine the distance from the nozzle exit to the LE of the cavity. This distance was a critical parameter of the cavity design because it determined the boundary-layer thickness at the cavity LE. A distance of 4 cm was selected, giving $Re_x = 7.6 \times 10^5$ at the cavity LE. Though lower than the Reynolds numbers used in other scramjet cavity simulations, the value is still high enough to be considered turbulent, as would be expected in a combustion chamber. This value of Reynolds number Re_x yields a wall Reynolds number of 1.2×10^5. The boundary-layer thickness at LE was calculated to be $\delta_t = 1.42$ mm using the turbulent, compressible boundary-layer theory outlined by Van Driest.[12] Van Driest's procedure employs an estimate from incompressible boundary-layer theory using an adjusted Reynolds number at the wall based on a power law approximation of Sutherland's viscosity law and the ideal gas law evaluated at the wall and referenced to the freestream. The boundary-layer thickness calculation was also compared to measurements and calculations performed by Latin[11] on the same facility and found to be within 6%.

The cavity dimensions were also selected to match those of similar experiments in the open literature. The cavity depth of 7.84 mm (Fig. 1) yields a depth/$\delta_t = 5.52$, which compares with the range of $1.38 <$ depth/$\delta_t < 9.25$ studied by others.[6,13,14] Because the tunnel width was fixed at 6.35 cm, this gives a width/depth ratio of 8.1, which was desirable to ensure two-dimensional flow in the cavity. This two-dimensional flow assumption was validated by recorded temperature data (see Experimental Results).

The forward portion of the acrylic cavity insert was designed to be recessed in the floor cavity, minimizing surface discontinuities upstream. This same recess in the tunnel floor also accommodated a flat plate insert that was used for establishing a reference data set. The thickness of the cavity insert (1.23 cm) was selected to ensure that during the 25-s test time the temperature gradient from the exposed upper surface would not propagate to the bottom side of the insert. This was done to ensure that the semi-infinite solid approximation used in the data reduction technique was accurate. The thermocouple at station 11, on the underside of the insert (Fig. 4), showed a 0.2°C temperature differential during tunnel operation, thus verifying the semi-infinite solid assumption. As shown in Fig. 4 and labeled according to Table 1, 11 type-T thermocouples were placed at various points of interest in the inclined trailing wall cavity. Three thermocouples (5, 9, and 10) across the span of the trailing wall were used to verify the two-dimensional flow assumption.

Cavity Assembly

The thermocouples were mounted flush to the surface of the insert using a commercially available epoxy adhesive. The importance of thermocouple juxtaposition to the surface is discussed further in the "Data Reduction" section. Holes through the acrylic insert 1 mm in diameter allowed the thermocouple wires to be fed to the A/D system.

Cavity Hardware

Type-T thermocouples, placed according to Fig. 4, were used to measure the surface temperature of the inclined trailing wall and flat plate cavity inserts. The thermocouple lead wires were 0.127 mm in diameter, with a bead diameter of approximately 0.254 mm. The thermocouples were calibrated at room temperature and at 16°C. The lower calibration temperature was chosen based on the lowest observed temperature during testing.

Experimental Procedure

Before each test, the cavity insert and interior tunnel walls were allowed to come to thermal equilibrium. This was verified by comparing the temperature readings of thermocouples at stations

Table 1 Cavity insert thermocouple locations

Description	Axial distance from cavity LE, cm	Station
Bottom	1.800	1
First position on incline	2.200	2
Second position on incline	2.533	3
Third position on incline	2.866	4
Center	3.200	5
Second from top	3.500	6
Top of incline	3.800	7
Top	4.750	8
Left	3.200	9
Right	3.200	10
Lower temperature	0.250	11

1, 8, and 11 (see Table 1). Once these temperature readings were the same (within 0.4°C), the data acquisition system was started. The vacuum tanks downstream of the diffuser were opened to the test section to evacuate the test section and plenum chamber. The high-pressure tank upstream of the plenum chamber was opened, beginning supersonic flow through the nozzle and test section. After approximately 25 s, the vacuum tanks were at nearly the same pressure as the high-pressure supply, ceasing supersonic flow through the test section. The data acquisition was terminated approximately 3 s after the flow ceased.

Data Reduction

The heat transfer coefficient was determined analytically using first principles. When a control volume analysis at the surface of the

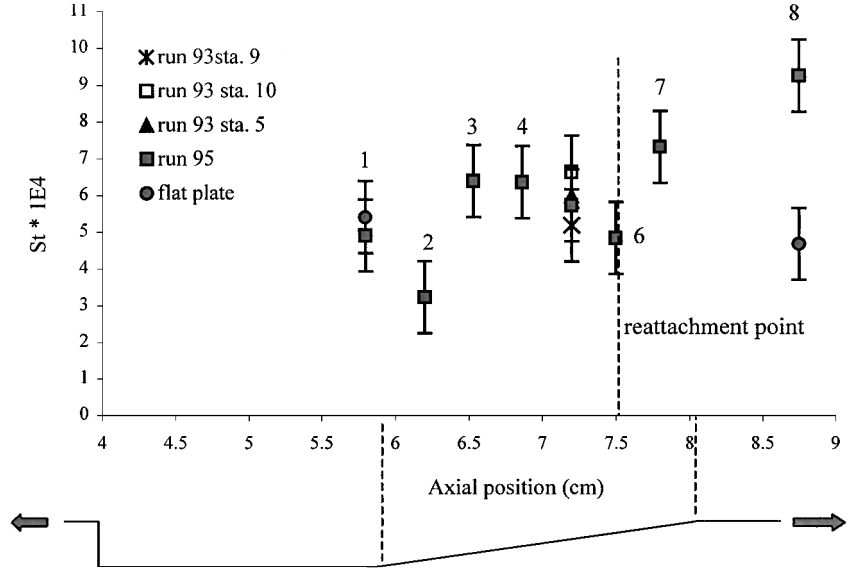

Fig. 3 Experimental Stanton number results, inclined trailing wall insert.

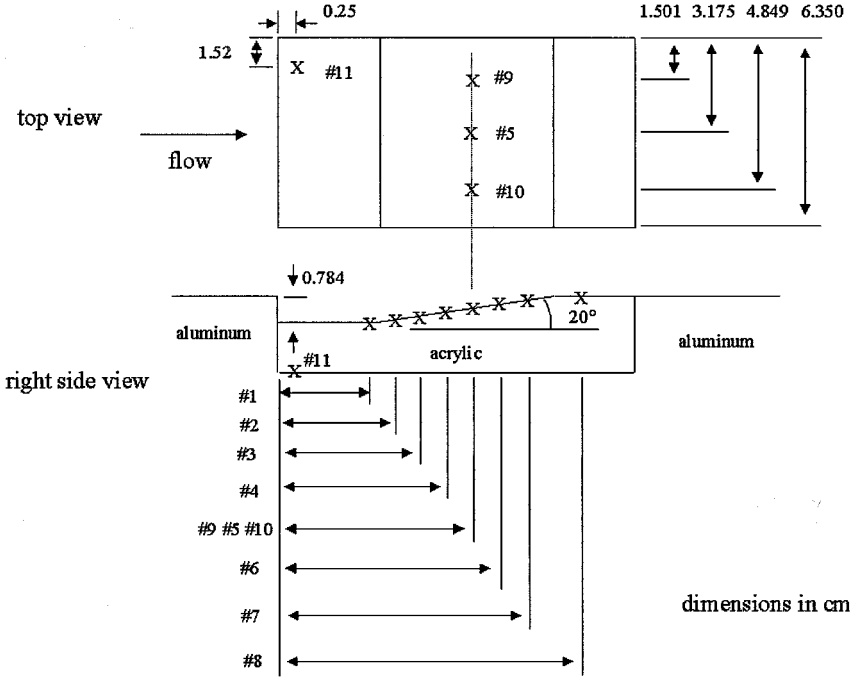

Fig. 4 Thermocouple placement.

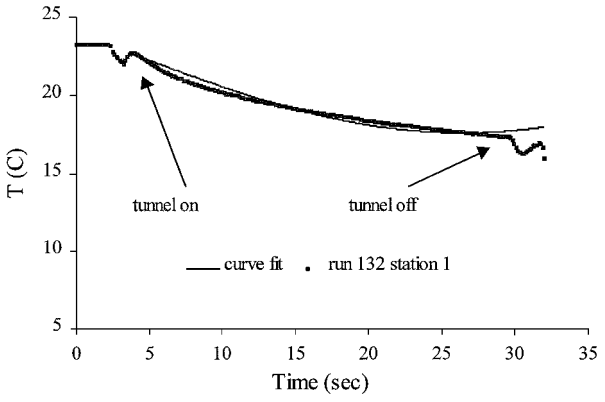

Fig. 5 Comparison between fit and recorded data for flat plate insert, station 1.

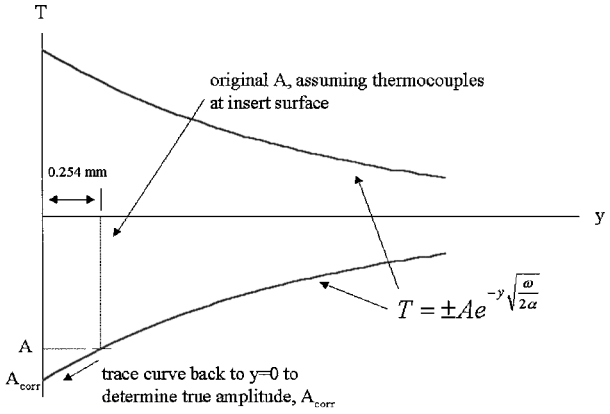

Fig. 6 Determination of corrected temperature amplitude.

acrylic insert is performed and heat transfer due to radiation and lateral conduction is neglected, the convective heat transfer coefficient can be written as

$$h = \frac{-k_{\text{acr}}(\delta T/\delta y)_{y=0}}{T_w - T_{\text{aw}}} \tag{1}$$

In early tests, it was observed that the surface temperature varied roughly as a quarter period of a sinusoid during the 25-s test time. Because a sinusoidal wall temperature variation has a direct analytical solution for surface heat flux (and, therefore, h), it was employed as the method to reduce the data and determine h.

A typical comparison between the sinusoidal curve fit and recorded surface temperature data (Fig. 5) shows good agreement during the tunnel operation time. Hence, a curve fit to the data was used to calculate the heat transfer coefficient through the systematic process outlined hereafter.

Assuming a periodic function for T_w, the temperature gradient at the surface, $\delta T/\delta y$ at $y = 0$, can be evaluated using the classical, one-dimensional, analytical solution for periodic temperature input at the surface of a semi-infinite solid[15]:

$$T_w(y, t) = A\exp(-y\sqrt{\omega/2\alpha})\cos\left[\omega t - (\omega/2\alpha)^{\frac{1}{2}}y + \phi\right] + T_i \tag{2}$$

When applied at the surface ($y = 0$), this temperature input becomes

$$T_w(0, t) = A\cos(\omega t + \phi) + T_i \tag{3}$$

and the corresponding surface gradient is

$$\left(\frac{\delta T}{\delta y}\right)_{y=0} = A\sqrt{\frac{\omega}{2\alpha}}[\sin(\omega t + \phi) - \cos(\omega t + \phi)] \tag{4}$$

The preceding formulation assumes that the solid beneath the surface of interest is at a uniform temperature T_i at $t = 0$ and that the solid can be considered semi-infinite. This general procedure of determining heat transfer coefficients using a curve fit to recorded surface temperatures has been employed successfully in gas turbine research.[16] A curve fit to the recorded temperature data was determined with appropriate selection of the temperature amplitude A, frequency ω, and phase shift ϕ, assuming that the thermocouples were positioned at the surface, that is, using Eq. (3). This selection was performed by varying A and ω until a minimum value of a least-squares fit was achieved over the tunnel operating time. However, the thermocouples could not be located exactly at the surface of the insert, and the actual temperature-sensing location was slightly below the surface. Therefore, the temperature amplitude required a correction to account for this small, but nontrivial, distance.

Measurements taken at several thermocouple stations determined the thermocouple bead placement relative to the insert surface to be 0.127 mm (±0.0127 mm). This distance was increased to include one-half of the bead diameter to better account for the actual thermocouple sensing location, yielding a distance of 0.254 mm. This distance was used to determine the corrected temperature amplitude with the curve fit temperature amplitude obtained from Eq. (2) in the manner described hereafter and shown schematically in Fig. 6.

First, the temperature amplitude A and frequency ω were determined by curve fit with the recorded temperature, as described. Then the corrected temperature amplitude A_{corr} was obtained by tracing the exponential component of Eq. (2) back to the ordinate axis by the known distance, that is, 0.254 mm. Only the exponential component of Eq. (2) was used because it represented the upper and lower bound (amplitude) for the periodic component. This corrected temperature amplitude was the actual surface temperature amplitude and was determined by

$$A = A_{\text{corr}}\exp(-y\sqrt{\omega/2\alpha}) \tag{5}$$

where ω was the same value as that determined by the curve fit and α was evaluated using the thermophysical properties of the acrylic: $\rho = 1185$ kg/m^3, $k = 0.16$ W/mK, and $c_p = 1069$ J/kgK (Ref. 17). With A_{corr} in place of A, Eqs. (3), (4), and (1) were then used to calculate the surface temperature, temperature gradient, and heat transfer coefficient, respectively. The adiabatic wall temperature T_{aw} in Eq. (1) was based on T_0 and M_∞ (Ref. 18). The Stanton number was determined from the heat transfer coefficient normalized by V_∞ and ρ and c_p evaluated at the reference temperature[18,19] of 235 K. To verify that the cosine curve fit method was reasonably appropriate, the h determined by the curve fit was found to be on the same order as the h determined by the numerical summation technique outlined by Schultz and Jones.[20]

Computational Setup

The computational facilities included a personal workstation and the commercially available software program, Fluent version 5.4. The computational results were obtained using a steady-state solution. As can be seen in Fig. 5, the tunnel surface temperature history is transient in nature. However, the schlieren flow visualization technique verified that the flow structure through the tunnel (shock patterns and shear layers) reached steady state within 2 s. Because these are presumed to be the primary physical mechanisms influencing surface heat transfer, the h calculated by the transient method was considered to be approximately equivalent to that which would be measured in a steady-state computational analysis. Therefore, a steady-state heat transfer solution was applied. A two-dimensional, coupled explicit solver, which solves the governing Navier–Stokes equations written in vector integral form, was chosen for the present work.

Two turbulence models were employed: one for the cavity case and one for the flat plate case. A standard k–ε model, with equations for turbulent kinetic energy and dissipation rate, was used for the flat plate case. A Reynolds' stress model (RSM) was used for the cavity case due to its ability to evaluate recirculating regions.[21]

The flat plate model case utilized standard wall functions, requiring that the wall coordinate y^+ be in the range of 30–60. For the cavity, the zonal wall treatment was used, requiring that y^+ be on the order of unity but not larger than 4–6. A second-order upwind discretization scheme was used for the flow, solid, and turbulence equations. Conduction through the solid was determined by Fourier's law.

The fluid inlet boundary conditions for the experimental test section (measured total pressure and temperature and calculated static pressure from isentropic flow tables for air, $\gamma = 1.4$) were used as the inlet boundary conditions and also provided the initial conditions for the entire computational domain. The inlet boundary conditions also included inputs for turbulent viscosity ratio and turbulence intensity from which the turbulence model calculates the required turbulent inlet quantities (k, ε, etc.). The turbulence intensity was 0.8% (Ref. 7), and the turbulent viscosity ratio was assumed to be 10. Air was the working fluid and was modeled as an ideal gas with molecular viscosity that followed Sutherland's law (with default coefficients) and with thermal conductivity and specific heat as piecewise linear functions of temperature.

As discussed earlier, the transient experimental test in the short-duration facility was intended to approximate the steady-state heat transfer behavior of the cavity. For heat flow to occur in the steady-state computational fluid dynamics (CFD) model, a constant temperature boundary condition was imposed along the outer horizontal boundaries of the upper and lower tunnel walls (Fig. 7). Because the largest temperature gradients were expected to be in the vertical direction in the solid, adiabatic wall conditions were imposed at the upstream and downstream vertical solid boundaries of the upper and lower tunnel walls (Fig. 7). These same solid and fluid boundary conditions were also imposed for the domain of the flat plate case.

The mesh for the flat plate and cavity cases was constructed using a structured quadrilateral grid with increased cell density along the tunnel wall to resolve the boundary layer. This increase in cell density was also used within the walls adjacent to the flow to better resolve the heat flux from the walls to the flow. Because of symmetry, only the lower wall was included in the domain for the flat plate case.

Convergence was verified by monitoring the solution residuals and the surface heat flux sum along the inclined trailing wall or along the tunnel floor for the flat plate insert. The final solution was determined when heat flux did not vary by more than 5% between grid adaptations and the residuals did not vary by more than 0.001.

Figure 8 shows a portion (approximately 15 cm) of the computational domain (55 cm) for the flat plate case. The final cell count was 22,400. The computational domain for the inclined trailing wall is shown in Fig. 7. The axial limits of the flow domain are the nozzle exit and a point 5.000 cm downstream of the cavity. This extra length downstream of the cavity was included to verify one-dimensional solid conduction and to allow sufficient domain for the boundary layer downstream of the cavity to develop. Note the grid refinement along the cavity walls to account for y^+ values. The wall cells were adapted based on the recommended range for y^+. The final cell count for the cavity case was 20,193, compared to approximately 5,700 cells for the flat plate case over the same axial distance.

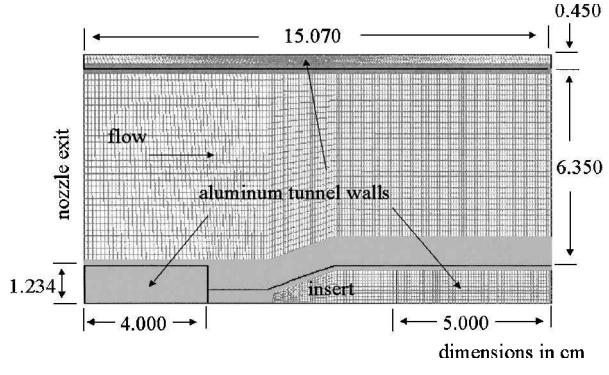

Fig. 7 Grid and computational domain for cavity with inclined trailing wall.

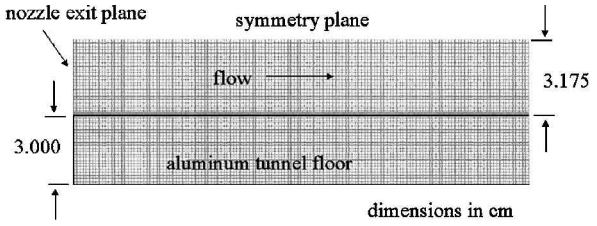

Fig. 8 Close-up of flat plate computational domain.

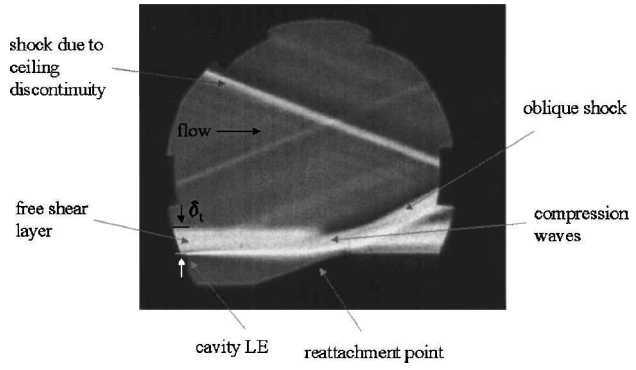

Fig. 9 Schlieren photograph showing flow reattachment and oblique shock formation.

Results and Discussion

Flow Visualization

A schlieren flow visualization technique was employed to elucidate the flow structure in and around the cavity. Figure 9 shows a schlieren photograph with a horizontal knife edge to capture vertical density gradients.

The expected shock angle for flow at Mach 2.9 incident on a 20-deg corner is 38.5 deg by the use of the oblique shock relations for air, $\gamma = 1.4$. The shock angle measured from the shear layer to the shock in Fig. 9 is 29 ± 2 deg. The free shear layer was used as the horizontal reference surface rather than the tunnel floor because the flow migrates into the cavity slightly with axial distance, as noted in the schlieren image. The reattachment point was 1.7 ± 0.1 cm, as measured from the beginning of the inclined trailing wall. This was deduced from Fig. 9 as the point where the lowest extreme of the shear layer intersects the inclined trailing wall.

The discrepancy between the experimental results and oblique shock theory may be partially explained by considering boundary-layer–shock interaction, a phenomenon unaccounted for in oblique shock theory. This boundary-layer–shock interaction can be seen in Fig. 9 above the reattachment point in the location of the compression waves. The curved appearance of the shock before it reaches its final angle may be due to the presence of a curved displacement surface near the top of the inclined trailing wall, as discussed hereafter.

From Fig. 9, it is clear that the flow coalesces into an oblique shock from a series of compression waves above the reattachment point. Settles et al.[6] postulate that this occurs due to a gently curved displacement surface formed by the free shear layer during the reattachment process on the inclined trailing wall. This trend in the displacement surface is shown in Fig. 10. Notice that the displacement thickness decreases along the inclined trailing wall in both the Settles et al.[6] data and the current CFD work. Settles et al. performed experiments in nearly identical conditions with $M_\infty = 2.92$ over a 20-deg inclined cavity wall. (The reattachment point, determined from the schlieren photograph, is included in Fig. 10 for clarity. The inclined wall position is measured from the inclined trailing wall–cavity floor junction along the inclined trailing wall.) The blockage associated with the displacement thickness can be thought of as an extension of the wall because no mass flow crosses the displacement

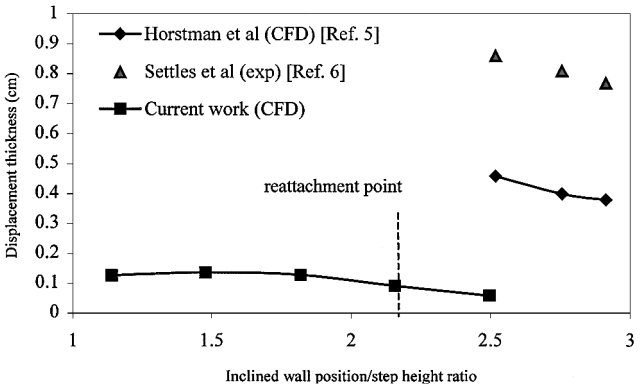

Fig. 10 Displacement thickness along inclined trailing wall.

thickness. Because the displacement surface is curved, it would gradually turn the flow, causing small disturbances or Mach waves to converge into an oblique shock outside of the boundary layer. With the CFD prediction of the displacement thickness distribution downstream of the reattachment point, a new equivalent inclined wall angle of 10.5 deg from horizontal can be computed, with a corresponding oblique shock angle of 28.5 deg. This is, of course, a very simplified analysis of the complex shock–boundary-layer interaction in the cavity, but it does demonstrate the expected magnitude of the effect.

With the schlieren image, the boundary layer at the cavity LE was estimated to be approximately 7.5 mm. This value is roughly five times thicker than the boundary layer determined by the method outlined by Van Driest.[12] However, Gessner et al.[22] showed that the boundary layer is approximately three times thicker along a corner bisector than along a wall bisector for square duct flow at similar inlet conditions. Because the schlieren image assumes two-dimensional flow across the tunnel width, it would capture this thicker boundary layer due to corner effects. Additionally, assuming constant static pressure through the boundary layer, the schlieren image would capture the thermal boundary layer which is slightly thicker than the velocity boundary layer. This can be seen in the Prandtl number (ratio of the momentum and thermal diffusivities), which is approximately 0.7 for air. Therefore, the boundary-layer thickness obtained from the schlieren image is not unreasonable.

Experimental Results

The Stanton number calculations were performed using the surface temperature history data. The variation of Stanton number with axial position for both cavity inserts is shown in Fig. 3, with the cavity geometry and station numbers included for clarity.

The two-dimensional flow assumption requires that the Stanton numbers at stations 9 and 10 be virtually the same as that at station 5 because they are at the same axial position. As shown in Fig. 3, the lateral variation in Stanton number is within the experimental uncertainty. After further inspection of Fig. 3, one will notice that the Stanton number at station 5 for run 95 and run 93 are nearly coincident. These two observations confirm that the tests were consistent and repeatable, respectively. The data indicate that the Stanton number at station 8 (the farthest downstream) is considerably higher than at any other station. Indeed, the Stanton number downstream of the oblique shock was found to be nearly 100% higher than that at the same axial location on the flat plate. This increase is thought to be due to the shock–boundary-layer interaction downstream of the inclined trailing wall.

The physical mechanisms of recirculation, reattachment, and stagnation flow are all evident in the Stanton number data shown in Fig. 3. The Stanton number increased nearly 20%, descending the inclined wall from reattachment. This was most likely due to recirculation and the associated change in fluid velocity magnitude and direction. Ascending the inclined trailing wall from reattachment, the Stanton number increased 50% between stations 6 and 7, with reattachment occurring between these stations. This increase was due to the conversion of kinetic energy to thermal energy associated with flow turning at the inclined trailing wall. This increase in Stanton number due to flow turning can also be seen from station 2 to station 1 (along the local reverse-flow direction) where the Stanton number increased more than 50%. The cavity floor at station 1 represents a 20-deg wedge to the flow moving down the inclined wall from station 2. An oblique shock wave did not result, however, because the local Mach number is apparently subsonic.

Computational Results

The oblique shock placement can be seen in Fig. 11 based on Mach number contours above and downstream of the top of the inclined trailing wall. With Fig. 11a, the shock angle was measured to be 28 ± 2 deg, again significantly reduced from the oblique shock value of 38.5 deg, but in good agreement with the schlieren results. Figure 11b shows a close-up of the cavity Mach number contours showing the presence of the coalescing Mach waves. The maximum reverse Mach number in the cavity, corresponding to the maximum reverse velocity of $0.17V_\infty$, is also shown. The reattachment point was located at a point 1.7 ± 0.1 cm along the inclined trailing wall, matching the experimental value exactly. This location was also confirmed as the point where c_f went to zero. The CFD results indicated two recirculation zones within the cavity, as depicted in Fig. 11b. This value is bounded by the results of others, as will be discussed later.

The shear layer reattachment point is one method of comparing the present results with the open literature. Horstman et al.,[5] in their computational model of the Settles et al.[6] experimental configuration, determined their reattachment point to be 5.2 cm from the cavity floor–inclined wall junction. The reattachment point-to-step height ratio for their study compares well with that for the present work, 2.05 vs 2.17, respectively. Although the configuration of Horstman et al.[5] was unique in that the inclined trailing wall continued beyond the floor level, this method of comparison is still reasonable given the findings of Samimy et al.[14] After careful comparison with other experiments involving free shear layers, the authors found that the geometry downstream of the reattachment point has little effect on the reattachment process.

The CFD results predicted a boundary-layer thickness at the cavity LE that was within 12% of that determined from the method shown by Van Driest[12] (1.42 vs 1.25 mm). Because a critical parameter governing the flow behavior is the cavity depth to δ_t ratio, this close match between the CFD and analytical results provides confidence that the cavity in the computational domain was exposed to the same inlet flow structure as that present in the wind tunnel.

The computational model prediction of Stanton number variation with position for the inclined trailing wall insert is shown in Fig. 12. The results shown in Fig. 12a show poor agreement. In fact, the computational results are as much as five times higher than the experimental results. This suggests that the turbulence model does not accurately calculate the energy transfer between the wall and the flow. However, the turbulence model did capture the bulk flowfield structure, such as reattachment point and boundary-layer thickness, as discussed earlier. Therefore, a modified Reynolds analogy[23] was employed to investigate this difference. The results using the modified Reynolds analogy shown in Fig. 12b show reasonably good agreement along the cavity floor and ramp. Incropera and DeWitt[23] discuss that this analogy has low sensitivity to pressure gradient in turbulent flow and remains approximately valid. The differences shown in Fig. 12a were, in part, attributed to the use of a constant reference (adiabatic wall) temperature in Eq. (1) (a variable reference temperature was not available for input to the computational analyses).

This unexpected discrepancy between the experimental and computational Stanton number results required further investigation. To this end, a CFD analysis of the flat plate insert heat transfer with a 3.000-cm-thick aluminum wall was compared to experimental Stanton number values determined using the sinusoidal curve fit method. A comparison of the Stanton number results in Fig. 13a shows poor agreement. However, the c_f distribution in Fig. 13b

Table 2 Comparison of results with the literature

	Reattachment point/step height ratio		Stanton number range (1*E*4)		c_f range (1*E*4)		Recirculation zone		Maximum reverse velocity; fraction of freestream	
Reference	Exp	CFD	Exp	CFD	Exp	CFD	Exp	CFD	Exp	CFD
Current work	2.17	2.17	0–9.3	0–51	——	0–32	——	2 (1 cw, 1 ccw)	——	0.17
Horstman et al.[5]	2.66 (Ref. 6)	2.05	——	——	0–1.3 (Ref. 6)	0–13	——	1 cw	——	0.17
Samimy et al.[14]	2.29	——	——	——	——	——	1 cw	——	0.2	——

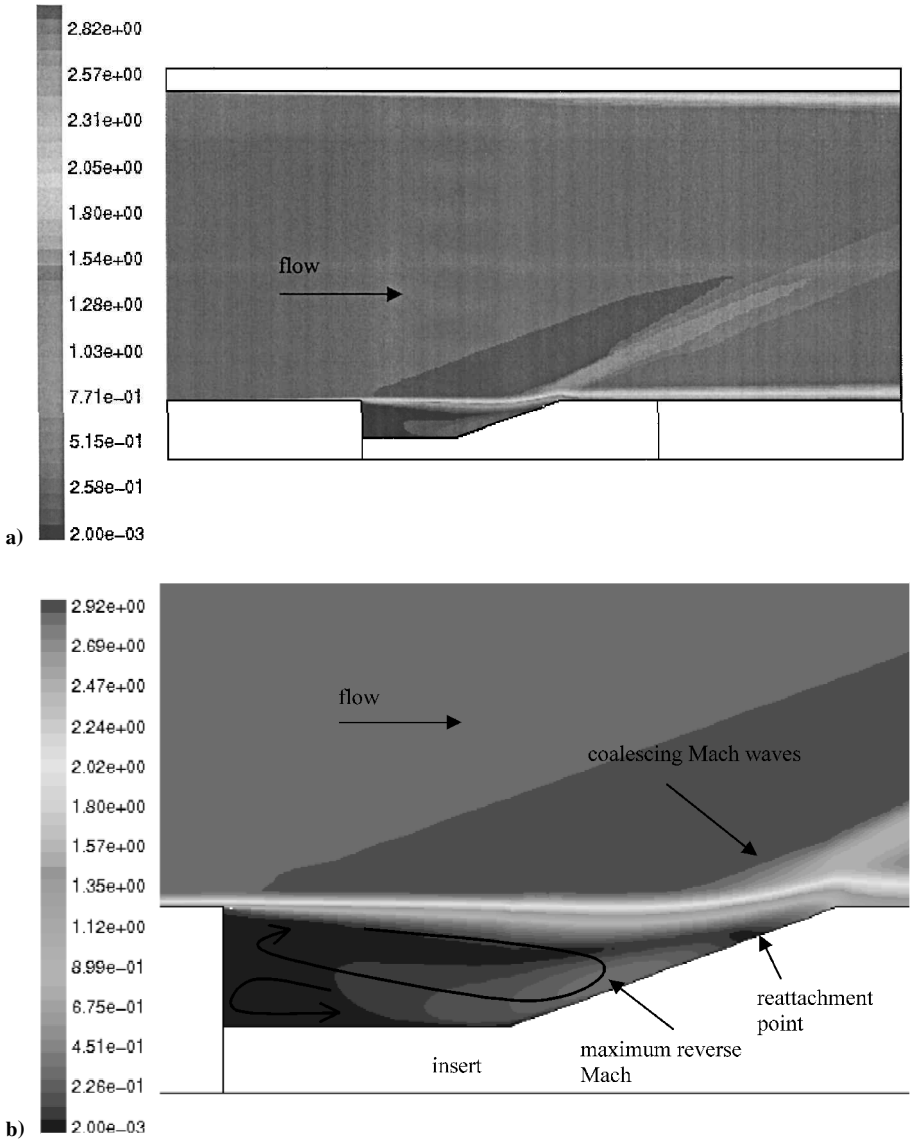

Fig. 11 Mach number distribution: a) through entire domain (upper) and b) through cavity.

shows reasonable agreement to the results of Latin.[11] Latin also determined the boundary-layer thickness using pitot data and color schlieren. At $x = 53.98$ cm from the nozzle exit, the boundary-layer thickness ranged from 6.9 to 13.8 mm for Latin's work and was 8.0 mm for the flat plate case. Latin did not make boundary-layer measurements in the region of the cavity used in this study. However, the CFD analysis predicted a 1.25-mm-thick boundary layer at the cavity LE, which was within 12% of that predicted by the method outlined by Van Driest.[12] These results indicate that the computational analysis did not accurately solve the conjugate heat transfer but may have, in fact, correctly determined the physical structure of the flowfield.

This discrepancy between the computational and experimental Stanton number results may be due to the choice of turbulence model. Although the computational and experimental shock angle and reattachment point results are in good agreement, the poor agreement in Stanton number results through the cavity suggests that the RSM model may not accurately model the near-wall physics as they relate to energy transfer. This limitation of current CFD models has been observed by others as well.

Table 2 shows a comparison between some experimental and computational results from the current work and those of other researchers. As indicated earlier, the cavity geometries and flow Mach numbers for both researchers shown in Table 2 were similar to the current geometry. Comparing the Horstman et al.[5] results to those of the current work, it is clear that the bulk flow motion (reattachment point) is well modeled, whereas the near-wall physics (c_f for Horstmann et al.[5] and Stanton number for the current work) is not.

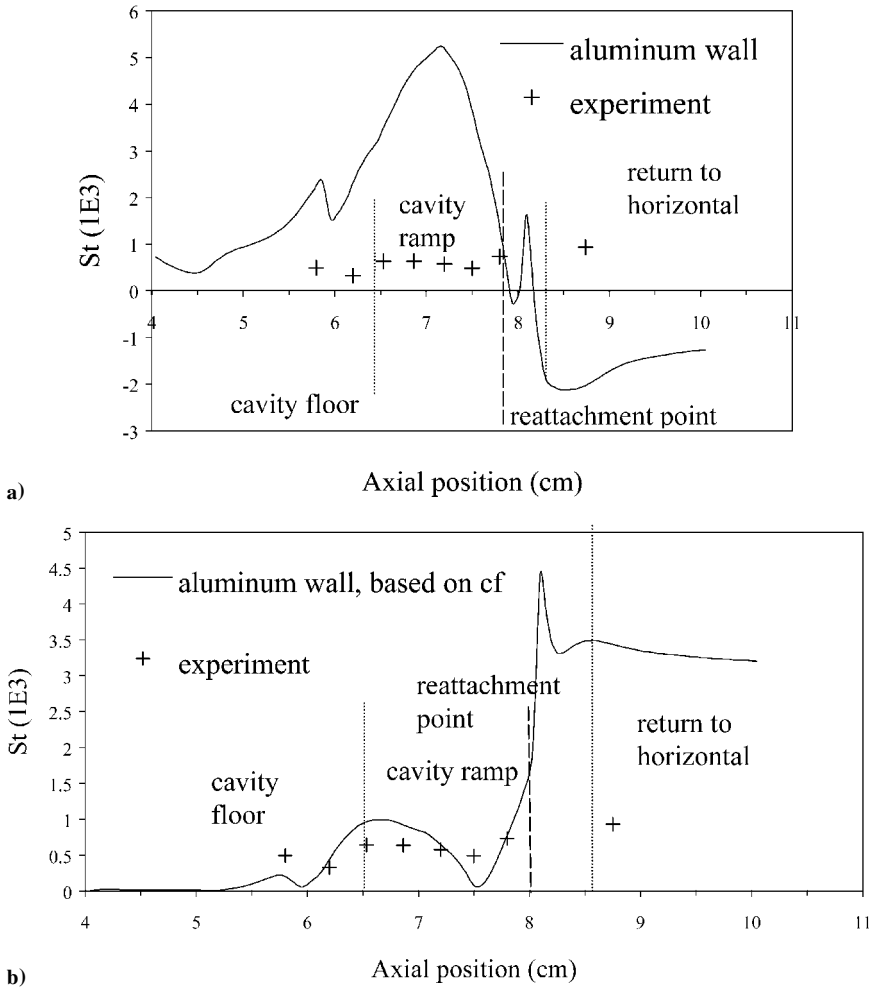

Fig. 12 Experimental and CFD Stanton number results for inclined trailing wall insert: a) based on computational heat flux (upper) and b) based on skin-friction coefficient.

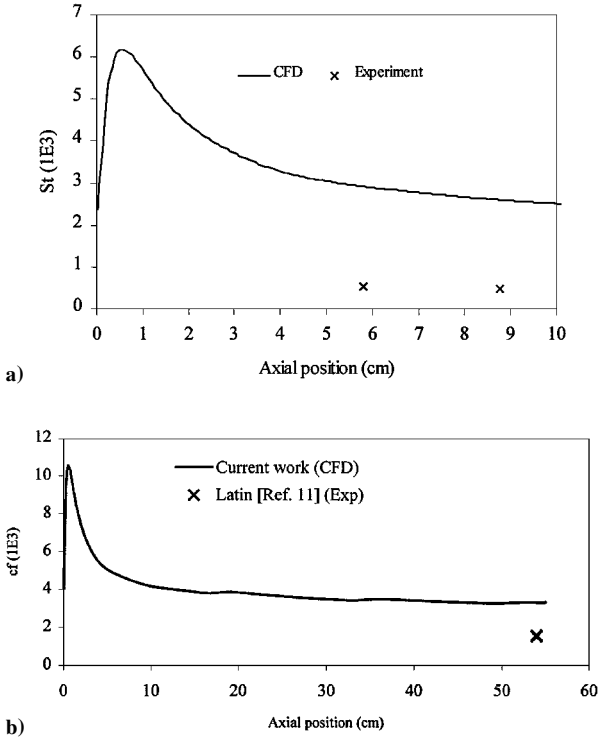

Fig. 13 Comparison of experimental and CFD data for flat plate insert: a) *St* distribution (upper) and b) c_f distribution.

This lack of an appropriate computational model for cavity flows can also be seen in the results of Weinberg et al.,[24] who performed a CFD analysis utilizing a standard $k-\varepsilon$ turbulence model based on the experimental research of Settles et al.[6] The results of Weinberg et al.[24] showed three recirculation zones (two clockwise and one counterclockwise) in the cavity. This result contradicts the results of Horstman et al.,[5] who used a Wilcox–Rubesin turbulence model, also based on the experimental results of Settles et al.,[6] and matched the one circulation zone observed experimentally. However, the CFD analysis of Horstman et al.[5] did not accurately predict the skin-friction coefficient on the inclined trailing wall, as noted earlier. Similar deficiencies were more recently echoed by Shih et al.,[25] who used a coupled $k-\varepsilon$ turbulence model, and Tam et al.,[26] who used a Baldwin–Lomax turbulence model for compressible flowfields. The differences between CFD and experimental results in each of these papers were noted by their respective authors, who universally concluded that further evaluation of turbulence models is required to more accurately predict cavity flows.

Conclusions

Heat transfer data in the form of Stanton number were determined for a cavity geometrically similar to one under review for use in a scramjet engine. The cavity geometry design incorporated an inclined trailing wall, which was designed to provide recirculation while minimizing the heat flux load to the trailing wall. The cavity Stanton number data were compared to data obtained for the same flow over a flat plate, as well as to data from a computational model. Comparisons were also made between the computed flow structure and experimental flow visualization. The following conclusions are presented based on the data:

1) Heat transfer downstream of the cavity was increased by nearly 100% compared to the flat plate case.

2) Heat transfer along the inclined trailing wall varied based on position relative to the flow reattachment point.

3) A curved displacement surface at the inclined trailing wall was proposed as a possible mechanism causing small compression waves to coalesce into an oblique shock. This shock–boundary-layer interaction was shown to account for an experimentally observed reduction in oblique shock angle from inviscid theory.

4) The turbulence models employed captured the cavity flowfield but underpredicted Stanton number by up to an order of magnitude.

Acknowledgments

The authors would like to thank Andrew Pitts, Department of Aeronautics and Astronautics, Air Force Institute of Technology (AFIT), for his assistance with the data acquisition and flow visualization systems. The assistance of the AFIT Machine Shop is also appreciated for the accurate and timely fabrication of the experimental model hardware.

References

[1]Sitz, J., "Hypersonic Experimental Research Vehicle," *NASA Dryden Flight Research Center*, URL: http://www.dfrc.nasa.gov/Projects/hyperx/x43.html [cited 15 Dec. 1998].

[2]Davis, D. L., and Bowersox, R. D. W., "Computational Fluid Dynamics Analysis of Cavity Flame Holders for Scramjets," AIAA Paper 97-3270, July 1997.

[3]Davis, D. L., and Bowersox, R. D. W., "Stirred Reactor Analysis of Cavity Flame Holders for Scramjets," AIAA Paper 97-3274, July 1997.

[4]Gruber, M. R., Baurle, R. A., Mathur, T., and Hsu, K.-Y., "Fundamental Studies of Cavity-Based Flameholder Concepts for Supersonic Combustors," AIAA Paper 99-2248, June 1999.

[5]Horstman, C. C., Settles, G. S., Williams, D. R., and Bogdonoff, S. M., "Reattaching Free Shear Layer in Compressible Turbulent Flow," *AIAA Journal*, Vol. 20, No. 1, 1982, pp. 79–85.

[6]Settles, G. S., Baca, B. K., Williams, D. R., and Bogdonoff, S. M., "Study of the Reattachment of a Free Shear Layer in Compressible Turbulent Flow," AIAA Paper 80-1408, July 1980.

[7]Huffman, R. E., "Mach 2.9 Investigation into the Flow Structure in the Vicinity of a Wrap-Around Fin," M.S. Thesis, AFIT/GAE/ENY/95D-13, School of Engineering, Air Force Inst. of Technology, Wright–Patterson AFB, OH, Dec. 1995.

[8]Powell, O. A., "Heat Transfer to the Inclined Trailing Wall of an Open Cavity," M.S. Thesis, AFIT/GAE/ENY/99M-07, School of Engineering, Air Force Inst. of Technology, Wright–Patterson AFB, OH, March 1999.

[9]*instruNet User's Manual*, Omega Engineering, Stamford, CT, 1998.

[10]*The Temperature Handbook*, Vol. 29, Omega Engineering, Stamford, CT, 1995, pp. 2–10.

[11]Latin, R. M., "The Influence of Surface Roughness on Supersonic High Reynolds Number Turbulent Boundary Layer Flow," Ph.D. Dissertation, AFIT/DS/ENY/98M-02, School of Engineering, Air Force Inst. of Technology, Wright–Patterson AFB, OH, March 1998.

[12]Van Driest, E. R., "Turbulent Boundary Layer in Compressible Fluids," *Journal of the Aeronautical Sciences*, Vol. 18, No. 3, 1951, pp. 145–160.

[13]Roshko, A., and Thomke, G. J., "Observations of Turbulent Reattachment Behind an Axisymmetric Downstream-Facing Step in Supersonic Flow," *AIAA Journal*, Vol. 4, No. 6, 1966, pp. 975–980.

[14]Samimy, M., Petrie, H. L., and Addy, A. L., "Study of Compressible Turbulent Reattaching Free Shear Layers," *AIAA Journal*, Vol. 24, No. 2, 1986, pp. 261–267.

[15]Arpaci, V. S., *Conduction Heat Transfer*, 1st ed., Addison Wesley, Longman, Reading, MA, 1966, pp. 280–282.

[16]Abuaf, N., Bunker, R. S., and Lee, C. P., "Effects of Surface Roughness on Heat Transfer and Aerodynamic Performance of Turbine Airfoils," American Society of Mechanical Engineers, Paper 97-GT-10, June 1997.

[17]Touloukian, Y. S., and Ho, C. Y. (eds.), *Thermophysical Properties of Matter*, Vol. 2, IFI/Plenum, New York, 1970, pp. 960, 961.

[18]Kays, W. M., and Crawford, M. E., *Convective Heat and Mass Transfer*, 3rd ed., McGraw–Hill, New York, 1993, pp. 380–388.

[19]White, F. M., *Viscous Fluid Flow*, 2nd ed., McGraw–Hill, New York, 1991, p. 511.

[20]Schultz, D. L., and Jones, T. V., "Heat-Transfer Measurements in Short-Duration Hypersonic Facilities," AGARDograph-AG-165, Feb. 1973, pp. 35–37.

[21]*FLUENT 5 User's Guide*, Fluent, Inc., Lebanon, NH, 1998, p. 9-9.

[22]Gessner, F. B., Ferguson, S. D., and Lo, C. H., "Experiments of Supersonic Turbulent Flow Development in a Square Duct," *AIAA Journal*, Vol. 25, No. 5, 1987, pp. 690–697.

[23]Incropera, F. P., and DeWitt, D. P., *Fundamentals of Heat and Mass Transfer*, 3rd ed., McGraw–Hill, New York, 1990, pp. 363, 364.

[24]Weinberg, B. C., McDonald, H., and Shamroth, S. J., "Navier–Stokes Computations on Aft End Flow Fields," AD-A115 796/XAG, May 1982.

[25]Shih, S. H., Hamed, A., and Yeuan, J. J., "Unsteady Supersonic Cavity Flow Simulations Using Coupled k–ε and Navier–Stokes Equations," *AIAA Journal*, Vol. 32, No. 10, 1994, pp. 2015–2021.

[26]Tam, C.-J., Orkwis, P. D., and Disimile, P. J., "A Comparison of Several Standard Turbulence Models for Two-Dimensional Open Cavity Flowfield Computations," AIAA Paper 95-0361, Jan. 1995.